CFA-18: a homochiral metal–organic framework (MOF) constructed from rigid enantiopure bistriazolate linker molecules†

Katharina Knippen,[a] Björn Bredenkötter,[a] Lisa Kanschat,[a] Maryana Kraft,[a] Tom Vermeyen,[b,c] Wouter Herrebout,[b] Kunihisa Sugimoto,[d] Patrick Bultinck[c] and Dirk Volkmer *[a]

In this work, we introduce the first enantiopure bistriazolate-based metal–organic framework, **CFA-18** (Coordination Framework Augsburg-**18**), built from the *R*-enantiomer of 7,7,7′,7′-tetramethyl-6,6′,7,7′-tetrahydro-3*H*,3′*H*-5,5′-spirobi[indeno[5,6-*d*]-[1,2,3]triazole] (*H*$_2$-*spirta*). The enantiopurity and absolute configuration of the new linker were confirmed by several chiroselective methods. Reacting *H*$_2$-*spirta* in hot *N*,*N*-dimethylformamide (DMF) with manganese(II) chloride gave **CFA-18** as colorless crystals. The crystal structure with the composition [Mn_2Cl_2(*spirta*)(DMF)$_2$] was solved using synchrotron single-crystal X-ray diffraction. **CFA-18** shows a framework topology that is closely related to previously reported metal–azolate framework (MAF) structures in which the octahedrally coordinated manganese(II) ions are triazolate moieties, and the chloride anions form crosslinked one-dimensional helical chains, giving rise to hexagonal channels. In contrast to MAFs crystallizing in the centrosymmetric space group $R\bar{3}$, the handedness of the helices found in **CFA-18** is strictly uniform, leading to a homochiral framework that crystallizes in the trigonal crystal system within the chiral space group $P3_121$ (no. 152).

Introduction

Metal–organic frameworks (MOFs) comprising azolate linker molecules often show excellent robustness against solvolytic or oxidative degradation.[1–3] Among these, triazolate-based linker molecules have recently gained particular attention due to their unique functional features, including quantum sieving,[3–6] sensing,[4,7] and activation of small molecules.[8,9] Because additional frameworks containing chiral information could find applications in, for example, enantioselective catalysis, drug delivery, gas storage, and separation,[10–14] this study aimed to implement robust chirality into bistriazolate-based MOFs.

There are various strategies for embedding chiral information into MOF structures.[13,15–17] It is possible to produce chiral information by spontaneous self-resolution[18] or to induce it[19,20] during crystallization, even when only achiral building blocks are used. The first chiral triazol-based MOF (**CFA-1**) was reported by our group in 2013.[18] This MOF is formed by the spontaneous crystallization of homochiral single crystals based on the solvothermal reaction of an achiral linker (1*H*,1′*H*-5,5′-bibenzo[*d*][1,2,3]triazole, *H*$_2$-*bibta*; Fig. 1)

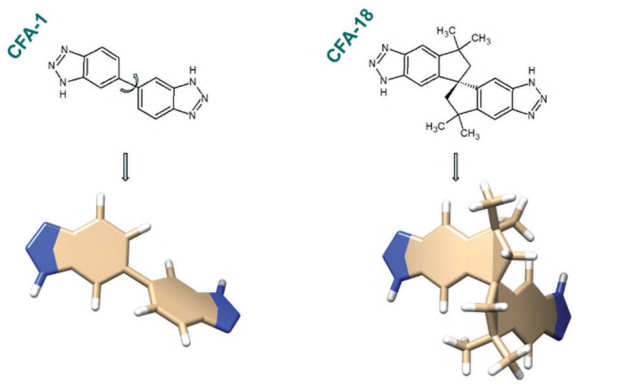

Fig. 1 Spatial arrangement of the linker molecules in **CFA-1** (left) and the rigid backbone of **CFA-18** (right).

[a]*Institute of Physics, Chair of Solid State and Materials Science Augsburg University, Universitätsstrasse 1, 86159 Augsburg, Germany.*
E-mail: dirk.volkmer@physik.uni-augsburg.de
[b]*Departement of Chemistry, University of Antwerp, Campus Groenenborger, Groenenborgerlaan, 171 G.V.018, 2020 Antwerp, Belgium*
[c]*Department of Chemistry, University of Ghent, Krijgslaan 281, S3, 9000 Ghent, Belgium*
[d]*Japan Synchrotron Radiation Research Institute, 1-1-1 Kouto, Sayo-cho, Sayo-gun, Hyogo 679-5198, Japan*

† Electronic supplementary information (ESI) available. CCDC2009784, 2009785, 2009786, 2009788 and 2009789. For ESI and crystallographic data in CIF or other electronic format see DOI: 10.1039/d0dt02847a

and zinc acetate dihydrate. During crystallization, the single bonds between the benzotriazole units of the linker molecule are fixed at a defined angle (42.1°). As a result, the coordinated *bibta* molecule adopts a fixed conformation and thus an axial chirality (Fig. 1), although the linker itself is achiral in the free state. Consequently, **CFA-1** consists of a racemic mixture of homochiral single crystals.[13,18] Subsequent attempts to alter the proportion of enantiomorphic crystals *via*, for example, chiral induction[19] have failed (*vide infra*).

In addition to post-synthetic modifications to introduce chiral information into MOFs, a safe route toward chiral azolate framework structures is the direct use of enantiopure azolate ligands.[10,13,15,21] However, since the synthesis of enantiopure organic linkers tends to be rather complex, most reported homochiral MOFs are based on naturally occurring enantiomeric building blocks[19,22] such as amino acids[10,11,13,23] and peptide derivatives as homochiral connectors.[24–26] Using the naturally occurring pool of chiral molecules certainly facilitates access to a huge variety of possible MOF structures, but because most amino acids are flexible, not stable concerning hydrolysis and pH sensitive,[13,25,26] creating stable homochiral MOFs with permanent porosity still remains a demanding challenge.[13,23]

For applications such as asymmetric heterogeneous catalysis, it is of great importance to control the pore size and flexibility of the crystal lattice. The integration of chirality into a rigid-backbone linker molecule is a promising strategy to produce stable framework structures with rational pore design.[17] One example of an inherently rigid building block is the spirobi(indan) building block, which is commonly used in the polymers of intrinsic microporosity (PIM) technologies.[14,27] This building block is equipped with an axial chirality similar to the BINOL backbone.[28] MOFs constructed from bistriazolate linkers often contain one of the following secondary building units (SBUs; Fig. 2). The first SBU contains a discrete pentanuclear coordination unit, which we refer to as a *Kuratowski-type SBU*.[3,29] The isoreticular frameworks MFU-4,[3] MFU-4l,[30] and **CFA-1**[18] (*cf.* Fig. 1), all of which contain zinc(II) ions, have been prepared from this SBU.

The second SBU type, termed metal–azolate framework (MAF), was first reported by Zhang *et al.*[31] in 2014 (*cf.* Fig. 3). The MAF-type SBU forms in the presence of metal ions other than Zn(II), namely Mn(II), Fe(II), and Co(II). Such trigonal MAF frameworks can be regarded as structural analogue of a framework type that forms from divalent metal ions and H_4dobdc (dobdc^{4-} = 2,5-dioxido-1,4-benzenedicarboxylate), which is synonymously referred to as MOF-74[32] or CPO-27.[33] As shown in the right side of Fig. 2, MAFs contain SBUs comprised of infinite one-dimensional helical strands of octahedrally coordinated metal(II) ions. The helix periodicity is three units per full 360-degree turn. Based on this, one can define a SBU containing three metal centers. Because MAFs crystallize in the centrosymmetric space group $R\bar{3}$, their unit cells contain helices with opposite turning sense.

Employing an enantiopure chiral spiro bistriazolate linker leads to the breaking of the centrosymmetry and the formation of a novel homochiral framework, which we refer to as **CFA-18**. This framework contains helical SBUs of only one turning sense, enforced by the chiral configuration of the linker molecules (*cf.* Fig. 7).

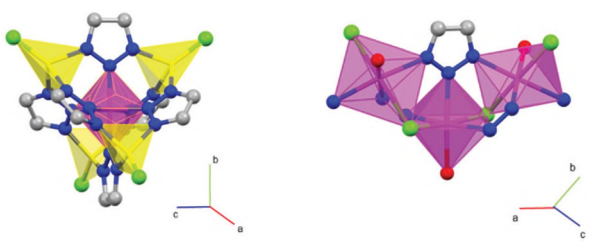

Fig. 2 Kuratowski-type SBU (left) and trigonal MAF-type SBU (right).

Results and discussion

Syntheses and characterization

The enantiopure H_2-*spirta* ligand (*aR*-**7**) and the racemic mixture (*rac*-**7**) were synthesized from bisphenol A in several steps (*aR*-**7**: 8, *rac*-**7**: 5). The synthesis of *rac*-**1** *via* the rearrangement of two bisphenol A molecules, nitration to *rac*-**4**, and Smiles rearrangement to *rac*-**5** followed by the reduction of the nitro groups (Schemes 1a, e, 2h and i) was described by Kumar *et al.*[34] The bis-triazoles **7** were obtained by the diazotation of **6** followed by ring closure (Scheme 2j). The isomers were separated by crystallizing the (−)-menthyl derivatives **2** (Fig. 5) from *n*-heptane (Scheme 1c)[29] and monitored by ^{1}H-NMR spectroscopy at the chemical shifts of 0.79, 2.27, 4.56, and 6.62 ppm (Fig. S3 and S4†). The enantiomeric excess of *aR*-**1** (ee 99%) and the final H_2-*spirta* ligand (*aR*-**7**) (ee 95%) was determined by high-performance liquid chromatography (HPLC; Fig. S2 and S25†). The yield of the nitro-diole *aR*-**4** was dramatically increased by reversing the cleavage of the (−)-menthyl groups and the nitration reaction steps (Scheme 1, *aR*-**2** to *aR*-**4**, steps d and e; overall yield of both steps: 29% ↔ steps f and g, overall yield of both steps: 94%). A further advantage of this method is the feasibility of synthesis at a larger scale because chromatographic purification is no longer required. The bottleneck of this synthetic route is the Smiles rearrangement. Batch sizes from 3–5 g nitrophenol **4** gave the corresponding nitroaniline **5** in moderate yields (60%–66%). Large-scale syntheses lead to immense losses in yield (10 g **4**: 30%; 20 g **4**: 10%). Because tetraamines **6** are slightly air sensitive, the filtration of the catalyst and removal of solvent after the hydrogenation step were performed under inert atmosphere, and the product was used immediately in the next reaction step.

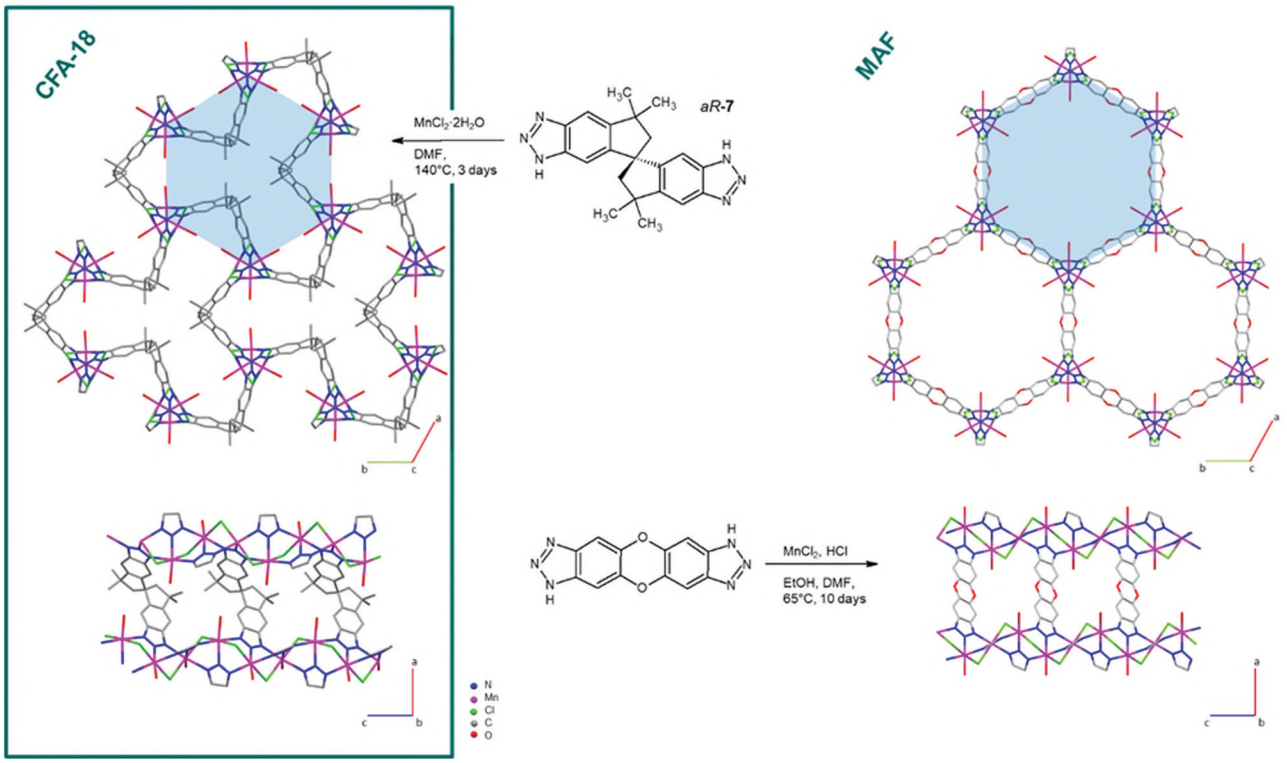

Fig. 3 Synthesis of $[Mn_2Cl_2(spirta)(DMF)_2]$ (**CFA-18**) (left) and comparison with traditional MAF structures $[M_2Cl_2(BTDD)(H_2O)_2]$, M = Mn(II),[2] Co(II),[1,2] Ni(II);[3] M = Cu(II) → MIT-20,[1] $[M_2Cl_2(BBTA)(H_2O)_2]$, M = Co(II);[2,7] M = Mn(II) → MAF-X27-Cl;[3]). The neutral ligand DMF is omitted for clarity.

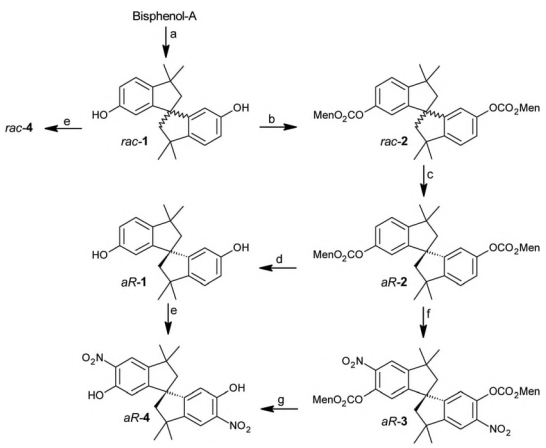

Scheme 1 Reaction sequence between bisphenol A and *rac*/*aR*-**4**: (a) methyl-sulfonic acid, 135 °C, 3 h; (b) ((–)-menthyl chloroformate, Et_3N, DMAP, CH_2Cl_2, 2 h, r.t.; (c) *n*-heptane, 39%, two steps (b and c); (d) hydrazine hydrate, THF, 3 h, reflux, 84%, (ee 99%); and (e) HNO_3 (70%).

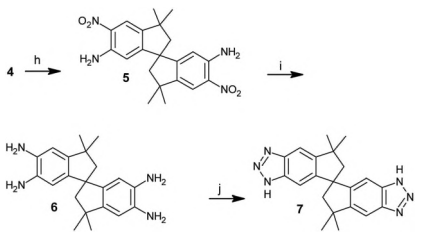

Scheme 2 Reaction sequence for *rac*/*aR*-**4** to *rac*/*aR*-**7**. (h) $ClCH_2CONH_2$, K_2CO_3, KI, DMF, 2 h, 90 °C, 3 h 150 °C, 66%; (i) Pd/C, H_2 (5 bar), EtOH, r.t., 24 h; (j) $NaNO_2$, H_3CCOOH, H_2O, 0 °C, r.t., 1 h, 82% (i + j).

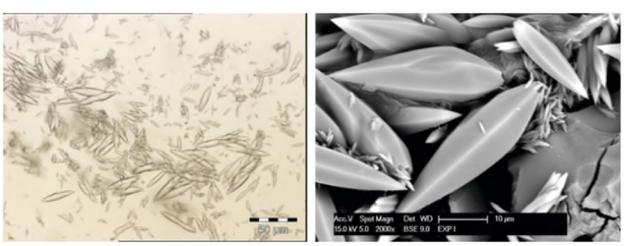

Fig. 4 Optical micrograph (left) and scanning electron microscopy images (right) of **CFA-18**.

All substances were characterized by ^{1}H- and ^{13}C-NMR spectroscopy along with CHN analysis, electrospray ionization (ESI)-mass spectrometry, melting point analysis, and polarimetry. Additionally, the structures of the nitroaniline intermediates **4** and the enantiopure *H*$_2$-*spirta* ligand (*aR*-**7**) were solved by single-crystal X-ray analysis.

Employing the enantiopure ligand (*aR*-**7**) in a solvothermal reaction with manganese(II) chloride dihydrate in *N*,*N*-dimethylformamide (DMF) at 140 °C resulted in the formation of colorless needle-shaped crystals of **CFA-18** with lengths up to 50 μm (Fig. 4).

Verification of absolute configuration

Finally, the absolute configurations of the enantiomers were determined by vibrational circular dichroism (VCD)[35,36] spectroscopy of the dinitrodiols *rac*-**4** and *aR*-**4** as well as the nitroamine derivates *rac*/*aR*-**5** and the final linkers *aR*-**7** in combination with the single-crystal structural analyses of compounds *aR*-**2**, **4**, and **7**.

Single crystals of *rac*- and *aR*-**4** were grown from CH_2Cl_2 *via* the slow evaporation of solvent. Single-crystal analyses revealed that compound *rac*-**4** crystallizes in the triclinic crystal system within the centrosymmetric space group $P\bar{1}$ (no. 2) (Fig. S32†), whereas *aR*-**4** shows higher symmetry and adopts an orthorhombic structure with the chiral space group $P2_12_12$ (no. 18) (Fig. S34†).

The absolute configuration of the *aR*-**4** structure with Flack-parameter 0.10(18) confirms the correct enantiomer form. Due to the use of Mo irradiation during the collection of X-ray data for the *aR*-**4** crystal (orthorhombic space group $P2_12_12$ (no. 18)), the Flack-parameter is not an unambiguous indicator of the absolute configuration.[19,37] However, the absolute configuration of the backbone can still be confirmed with complete certainty since the configuration of the menthyl protecting group in the structure of compound *aR*-**2** corresponds the configuration of (−)-menthyl chloroformate used in the synthesis of *aR*-**2** (Fig. 5).

The final linker (*aR*-**7**) was obtained from a H_2O/EtOH (50 : 1) solution by slow evaporation. Compound *aR*-**7** crystallizes within the high symmetrical trigonal chiral space group $P3_121$ (no. 144, Fig. S36†). A more comprehensive description and all crystallographic data of *rac*-**4**, *aR*-**4**, and *aR*-**7** can be found in the ESI† (chapter 4).

To verify the absolute configuration of the linker's spiro backbone, the infrared (IR) and VCD (Fig. 6, S26, and S27†) of the following compounds (enantiopure and racemic) were recorded and calculated: *aR*-**4** (Fig. S26†), *aR*-**5** (Fig. S27†), and

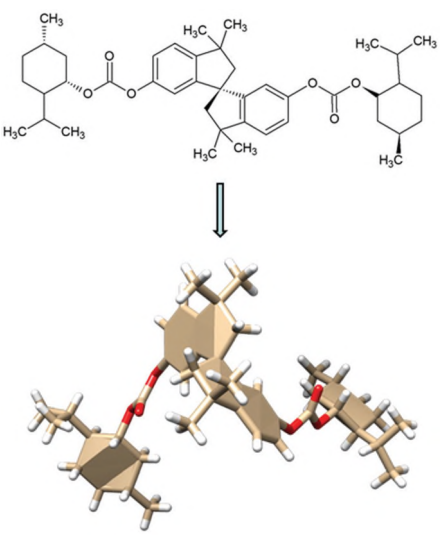

Fig. 5 Spatial arrangement of the intermediate *aR*-**2**.

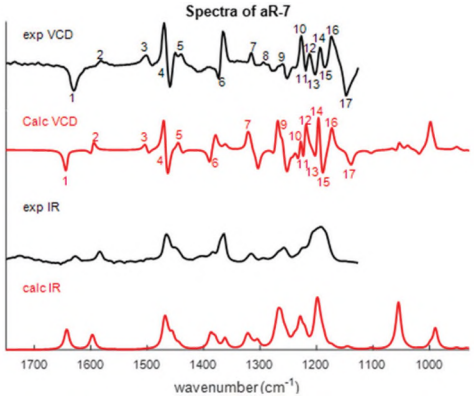

Fig. 6 From top to bottom, the experimental VCD spectrum, calculated VCD spectrum, experimental infrared spectrum, and calculated infrared spectrum of *aR*-**7**. A global shifting factor of 0.98 was used for the calculated spectra.

aR-**7** (Fig. 6). The spectra of *aR*-**4** and its racemate were recorded in $CDCl_3$. Due to the limited solubility of *aR*-**5** and *aR*-**7** in $CDCl_3$, the spectra of *aR*-**5** and *aR*-**7** and their corresponding racemates had to be recorded in DMSO-d_6 Solvent reference IR spectra were subtracted from all IR spectra recorded from solutions of the compounds, while the VCD spectra of the racemates served as references for the VCD spectra of *aR*-**4**, *aR*-**5**, and *aR*-**7**. The concentrations (26 mg mL^{-1}, 23 mg mL^{-1}, and 110 mg mL^{-1} for *aR*-**4**, *aR*-**5**, and *aR*-**7**, respectively) were chosen to yield an optimal signal-to-noise ratio.

Since the compounds are expected to be rather rigid, the conformational search variables were restricted to different rotational angles of the hydroxyl and amine groups. The actual search was accomplished using the Spartan software package.[38] For *aR*-**4**, albeit four unique conformations were identified, only a single conformation was found to have a Boltzmann weight above 0.001%. For *aR*-**5**, only a single conformation was found. For *aR*-**7**, all possible tautomers had to be considered due to the presence of the (protonated) triazole rings. Regarding the molecular symmetry, six unique tautomers were identified. The IR and VCD spectra of *aR*-**4** (Fig. S26†) and *aR*-**5** (Fig. S27†) were obtained by performing a geometry optimization followed by IR and VCD spectral calculations using Gaussian16[39] (b3lyp/aug-cc-pvdz with implicit solvation using the polarizable continuum solvent model[40]). The spectra of all unique tautomers of *aR*-**7** were calculated in the same manner and averaged using their enthalpy-based Boltzmann weights. Due to symmetry, certain tautomers could be generated in two different ways by changing the position of the hydrogen atom in either of the triazole groups. To account for this degeneracy, a statistical weight factor correction factor of 2 was introduced during the Boltzmann weighting. Lorentz broadening was performed on the line spectra using a full width at half maximum (FWHM) of 10 cm^{-1}. The calculations were performed for the *R* configurations of the spiro compounds.

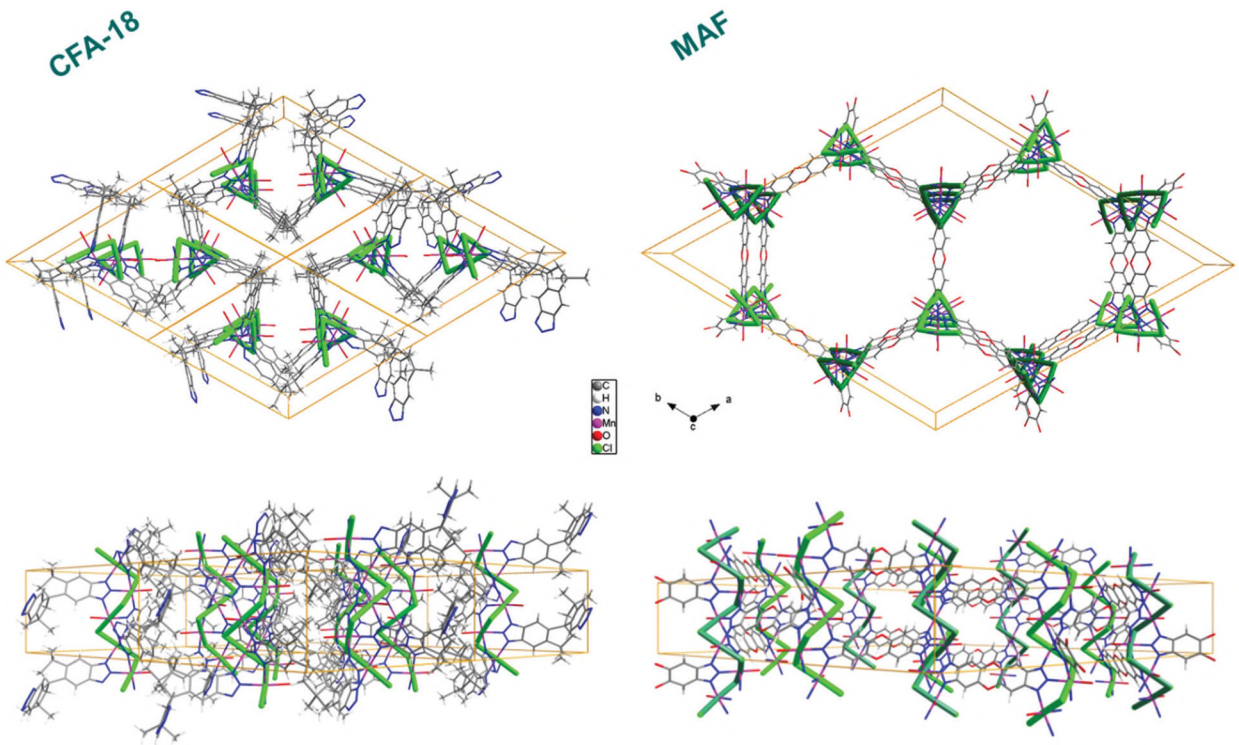

Fig. 7 Enantiopure (*P*) helical SBU of $[Mn_2Cl_2(spirta)(DMF)_2]$ (**CFA-18**) in comparison to the racemic helical SBU of conventional structures ($[M_2Cl_2((BTDD)_2(H_2O)_2]$, M = Mn(II),[2] Co(II),[1,2] Ni(II);[3] M = Cu(II) → MIT-20,[1] $[M_2Cl_2(BBTA)\text{-}(H_2O)_2]$, M = Co(II);[2,7] M = Mn(II) → MAF-X27-Cl;[3] right).

The bands in the VCD spectra were labelled by performing manual assignment in accordance with the IR spectra. As enantiomers have mirror-image VCD spectra, if the calculated VCD spectrum of a certain configuration matches the experimental VCD spectrum, the compound can be identified as consisting mainly of that configuration.

For *aR*-**4** (Fig. S26†), the general agreement between the computed and experimental VCD patterns is satisfactory, with most bands being predicted and having the proper sign. The predicted VCD spectrum of *aR*-**5** matches extremely well with the experimental spectrum. The same holds true for *aR*-**7**, with only a small band (band 8) in disaccord. Thus, based on VCD spectroscopic analyses, the absolute configuration of all three enantiopure compounds can be confidently identified as the *R*-configuration.[35,36,41]

Crystal structure analysis of CFA-18

Synchrotron single-crystal X-ray diffraction analysis revealed that **CFA-18** crystallizes in a trigonal crystal system in the chiral space group $P3_121$ (no. 152) with unit cell dimensions a = 17.344 Å, b = 17.344 Å, c = 8.807 Å, and $\alpha = \beta = 90°$ and $\gamma = 120°$. The crystal shows perfect merohedral twinning caused by 180° rotation around [001], thus simulating hexagonal symmetry. The asymmetric unit consists of one manganese(II) ion coordinated by one half of a linker molecule (1/2 spirta ≙ $C_{11}H_{11}N_3$), one chloride ion, and one DMF molecule.

An Ortep-style plot of the asymmetric unit of **CFA-18** with atom labels is shown in Fig. S37.† Tables containing the atomic coordinates as well as the bond lengths and angles are presented in Tables S17–S20†).

At room temperature, the experimental powder X-ray diffraction pattern of the bulk sample shows very good agreement with the simulated pattern based on the single-crystal structure analysis (Fig. 8). The unit cell parameters were determined by TREOR90[42] based on the recorded powder diffraction pattern: $a = b$ = 17.434(7) Å, c = 8.813(5) Å, unit cell volume = 2319.66 Å^3, $M(19)$ = 18, and $F(19)$ = 23 (0.015764, 54). These parameters are in good agreement with those derived from

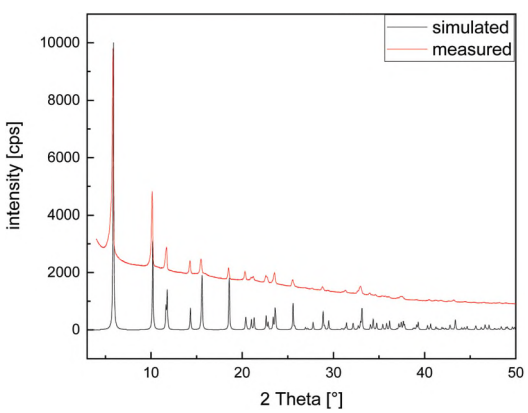

Fig. 8 Experimental and simulated powder X-ray diffraction patterns of **CFA-18**.

low-temperature single-crystal measurement. This affirms the phase purity of the material.

The SBU of **CFA-18** comprises a (*P*) helical chain (Fig. 3 and 7)[28] of three octahedrally coordinated manganese(II) ions bridged by μ_2-chloride ions. The metal and halogenide ions thus form one-dimensional strands that extend along the *c*-direction of the crystal lattice. These strands become three-dimensionally crosslinked by *spirta* molecules, pointing toward the symmetry-related *a*- and *b*-directions of the trigonal lattice. The framework composed of coordinated linker molecules and metal and halogenide ions forms narrow one-dimensional channels running in parallel to the *c*-lattice vector. Access to the channels is blocked by bound DMF molecules, which complete the coordination environments of the framework's manganese centers. Neglecting the coordinated DMF molecules, the potential average width of each channel and surface area were calculated to be approximately 4.5 Å and 1582.36 $m^2\ g^{-1}$ using the programs Poreblazer[43] and iRASPA,[44] respectively, assuming all DMF molecules were removed. However, all attempts to remove the coordinated solvent molecules *via* thermal activation procedures have failed, leading to the irreversible decomposition of the framework. Hence, the calculated porosity of the as-synthesized framework is vanishingly small (*cf.* Fig. S39†).[43,44]

CFA-18 framework stability analysis

The structural and thermal stabilities of **CFA-18** were determined with thermal gravimetric analysis (TGA; Fig. 9) in combination with variable temperature X-Ray powder diffraction (VTXRPD; Fig. 10). The TGA results obtained under flowing nitrogen gas show three weight-loss steps. The major weight-loss step (23.24 mass percent) at 150 °C–300 °C is related to the removal of DMF molecules and is in good agreement with the mass of two DMF molecules per unit, leaving the framework.

Solvent removal was monitored by Fourier transform IR (FTIR) measurements (Fig. S28†). The intense band at 1658 cm^{-1} corresponds to the C═O stretching vibration and is

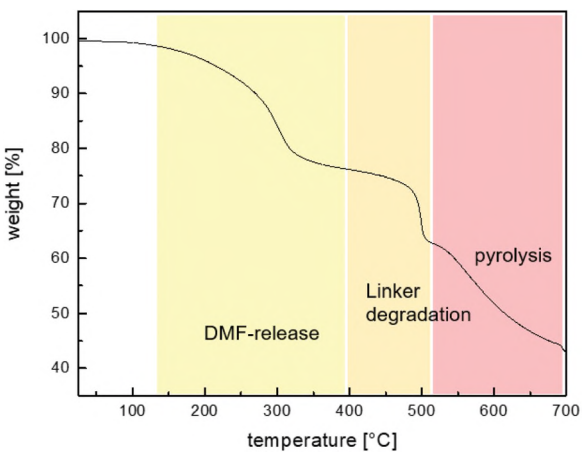

Fig. 9 TGA curve of **CFA-18**.

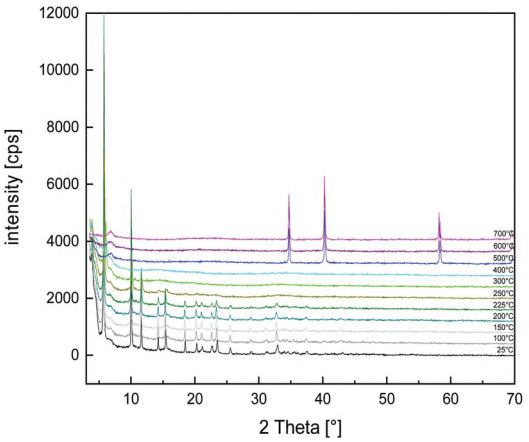

Fig. 10 VTXRPD pattern of **CFA-18**.

assigned to the coordinated DMF–ligand.[29] The band intensity decreases upon heating the material to $T > 153$ °C. Despite all the efforts, DMF could not be completely removed without destroying the crystal structure. Attempts to create free pore volume or free coordination sites by stepwise solvent exchange according to Howarth *et al.*[45] with water, dichloromethane, acetone, ethanol, and methanol also failed. In addition, solvent exchange experiments showed that the MOF is unstable in all these solvents. The product obtained after the complete evaporation of DMF shows no Bragg reflections, indicating a complete loss of crystallinity (Fig. 10). At 500 °C–510 °C, the weight loss (13.31%) is more abrupt, suggesting the thermal decomposition of the *spirta* linker. In the temperature range of 510 °C–700 °C, a further weight loss of 18.6% is observed, which corresponds to manganese oxide (9864-ICSD[46]). VTXRPD measurements (Fig. 10) confirmed the TGA results. At room temperature, the experimental powder diffraction pattern of the bulk sample shows very good agreement with the simulated pattern based on the single-crystal structure. The powder diffraction patterns show stable crystallinity at temperatures up to 150 °C. Above this temperature, the intensities of the diffraction peaks, especially those at 2θ values above 25°, decrease, indicating a loss of long-range order. At 300 °C–500 °C, the powder diffraction pattern lacks any Bragg reflections, demonstrating that **CFA-18** becomes completely amorphous upon losing the coordinated DMF molecules. At temperatures exceeding 510 °C, a new crystal phase appears, which can be assigned to manganese(II) oxide.

According to the TGA and VTXRPD data, the thermal decomposition of **CFA-18** occurs at 150 °C. This unexpectedly low thermal stability led us to analyze the structure of the bridging *spirta* linker moieties in more detail. A comparison of the geometric parameters of the coordinated linker molecules in the single-crystal structure of **CFA-18** with the quantum mechanically calculated parameters for the main tautomer of the pure *H*$_2$-*spirta* (*aR*-7) indicates that the coordinated linker is held in a firmly constrained state. As a measure of this

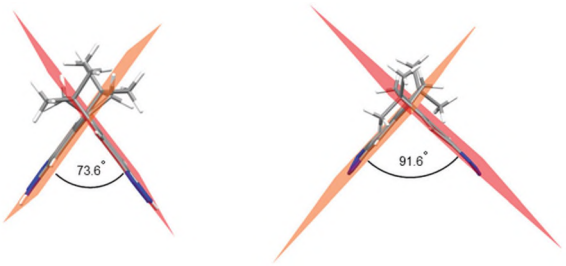

Fig. 11 Angles of the backbone in free H_2-*spirta* based on the quantum mechanically calculated main tautomer structure used in VCD analysis (left) and coordinated *spirta* (right).

tension, the angle spanned between the two independent planes running through the aromatic moieties are largely different. Whereas the angle in pure H_2-*spirta* (Fig. 11, left) is approximately 73.6°, the corresponding angle in the coordinated state (*i.e.*, in **CFA-18**) is approximately 91.6° (Fig. 11, right).

This steric strain might explain the low thermal stability of the framework. Nevertheless, the angles and bond lengths in the SBU are in good agreement with the known MAF structures reported in the literature;[1,31] the chloride bridges show a Mn–Cl–Mn angle of 93.05°, the bridging angle of Cl–Mn–Cl has a value of 175.69°, and the angle between manganese ion and the coordinated N-donor atoms of adjacent triazolate linkers (N–Mn–N) is approximately 85.4°. These angular values indicate a moderate deviation from perfect octahedral (micro-) symmetry. The bond distance between nitrogen and manganese (Mn–N) amounts to 2.136 Å, whereas the Mn–Cl distance is approximately 2.5 Å.

Conclusions

In this work, we established an organic synthesis for an enantiopure bistriazolate-functionalized spirobi(indeno) ligand (H_2-*spirta*) starting from the commercially available and inexpensive starting material bisphenol A. All reaction steps were optimized, resulting in good yields. The final linker, which was obtained after eight rapid synthetic steps, shows axial chirality and possesses high enantiomeric excess (ee 95%). Its absolute configuration was verified by X-ray structure analysis and VCD spectroscopy.

Since there are various strategies for embedding chiral information into MOF structures, the most promising of which is the direct use of chiral building blocks,[13,15–17] the integration of chirality into a rigid-backbone linker molecule is a promising strategy to produce stable framework structures with rational pore design.[17]

Using H_2-*spirta*, a homochiral spiro(indan)-based rigid-backbone linker molecule, we synthesized and characterized the first enantiopure homochiral triazolate-based MOF, **CFA-18**. This manganese(II)-containing framework crystallizes within the chiral space group $P3_121$ (no. 152). Owing to the steric strain of the coordinated linkers, the framework shows only moderate thermal stability (up to 150 °C). The knowledge gleaned from this study provides valuable insights for the future design of robust, hydrolysis stable homochiral MOFs.

Future approaches, including the use of different (transition) metal ions, for enhancing thermal stability and extending the length of the spiro linkers to relieve strain in the crystal packing arrangement might provide further interesting candidate homochiral MOFs for various enantioselective applications.

Experimental section

Materials and methods

All starting materials were of reagent grade and used as received from the commercial supplier. Melting points were measured with a Krüss KSP1N melting point meter. NMR spectra were recorded on a Mercury plus 400 high-resolution system (Fa. Varian Deutschland GmbH). ^{1}H NMR (400 MHz) and ^{13}C NMR (100 MHz) chemical shifts are given in ppm relative to the solvent signal. Molecular masses were determined with a Q-Tof Ultima mass spectrometer (Micromass) equipped with an ESI source. HPLC analysis was performed by a HITACHI system consisting of a pump with a degasser (L-2130), diode array detector (L-2455), column oven (L-2300), and autosampler (L-2200). A chiral analytical (5 μm, 4.6 × 250 mm) stationary phase (CYCLOBOND® I 2000 RSP, Astec®) was applied, and solvent mixtures of acetonitrile and 20 mM NH_4OAc at pH 4.0 (HPLC quality) were used. Compound *aR*-**7** was measured with a flow rate of 1 mL min^{-1} and an injection volume of 10 μL. Compound *rac*-**7** was measured with an injection volume of 40 μL. Saturated solutions of compounds *rac*-**1** and *aR*-**1** where both measured with a flow rate of 0.8 mL min^{-1} and an injection volume of 20 μL. Optical purities were determined by the analytical HPLC analysis of the resolved material. Thin-layer chromatography was conducted with silica gel F_{254} on Al foil (Merck). Gravity column chromatography was conducted with silica gel 60 (∅ = 0.063–0.200 mm; Merck). Elemental analysis was performed on a Vario EL III elemental analyzer (Elementar-Analysensysteme GmbH). Fourier transformed (FTIR) spectra were recorded in the range of 4000–400 cm^{-1} on a Bruker Equinox 55/Cary 630 FTIR spectrometer. IR and VCD spectra were recorded using a BioTools dual-photoelastic modulator (PEM) Chiral*IR*-2X™ spectrometer. The PEMs were optimized for 1400 cm^{-1} using a resolution of 4 cm^{-1}. The cell consisted of BaF_2 windows and had a path length of 0.100 mm. The concentrations were chosen to optimize the signal-to-noise ratio. The optical rotations were measured using a Jasco P-2000 polarimeter using standard conditions (25.00 °C, 589 nm). The rotational value was the average of at least 15 consecutive measurements. The diols *rac*-**1** and *aR*-**1** along with the (−)-menthyl esters *rac*-**2** and *aR*-**2** were synthesized from commercially available bisphenol A.[47] The nitrophenols *rac*-**4** and *aR*-**4** (Scheme 1e; alternative route) were synthesized *via* the nitration of *rac*-**1**.[48] TGA was per-

formed with a TGA Q500 analyzer in the temperature range of 25 °C–700 °C under flowing nitrogen at a heating rate of 5 K min^{-1}. Energy-dispersive X-ray spectroscopy was performed using a Philips XL 30 FEG scanning electron microscope equipped with an SiLi detector. Argon gas sorption measurements where conducted at 77 K with a Quantachrome Autosorb-I ASI-CP-8 instrument. X-ray powder diffraction (XRPD) data were collected in the 5–50° 2θ range using a Seifert XRD 3003 TT – powder diffractometer with a Meteor1D detector operating at room temperature using Cu Kα1 radiation (λ = 1.54187). Variable temperature X-ray powder diffraction (VTXRPD) measurements were collected in the 2θ range of 5–70° with 0.02° steps with a Empyrean (PANalytical) Diffractometer equipped with a Bragg-BrentanoHD mirror, a PIXcel3D 2 × 2 detector and a XRK 900 Reactor chamber (Anton Paar).

Single-crystal X-ray diffraction analyses of *aR*-2, *rac*-4, *aR*-4, and *aR*-7

The X-ray data for the single-crystal structure determinations of intermediates were collected using a Bruker D8 Venture diffractometer at −173 °C. Intensity measurements were performed using monochromated (doubly curved silicon crystal) MoKα radiation (0.71073 Å) for *rac*-**4**, *aR*-**2** and *aR*-**7**. Monochromated CuKα radiation (1.54178 Å) was used for the single-crystal investigation of *aR*-**4**. Integrated intensities and unit cell refinements were performed using the Bruker SAINT software package. The structures were solved by direct methods and refined using the SHELXL-97 program.[49]

Single-crystal X-ray diffraction analysis of CFA-18

Synchrotron X-ray data for single-crystal structure determination were collected at −173 °C on a Rigaku Saturn 724 diffractometer with a Si(111) channel-cut monochromator using RAPID-AUTO. The structure was solved by direct methods and refined using the SHELXTL program[49] with space group $P3_121$. The twin matrix (−1 0 0 0 −1 0 0 0 1) was applied for refinement, resulting in a BASF factor of 0.50(1), thus showing an equal part of each twin component. Multiple restraints were applied to the bond distances and angles of the linker and DMF molecules. Due to the small scattering contribution of the linker molecules, the positions of carbon atoms could only be refined isotropically. Hydrogen atoms were calculated using a riding model. The crystallographic data of **CFA-18** are presented in Table 1. Deposition numbers CCDC 2009784–2009789 contain the supplementary crystallographic data for this paper.†

Linker synthesis

3,3,3′,3′-Tetramethyl-2,2′,3,3′-tetrahydro-1,1′-spirobi[indene]-6,6′-diol (1).[47] M.p. (*rac*-**1**): 215 °C; M.p. (*aR*-**1**): 160 °C; ^{1}H NMR (400 MHz, d_6-DMSO, 20 °C) δ 9.00 (s, 1H), 6.99 (d, ^3J = 8.4 Hz, 1H), 6.58 (dd, ^3J = 8 Hz, ^4J = 2.4 Hz, 1H), 6.10 (d, ^4J = 2.4 Hz, 1H), 2.25 (d, J = 12.8 Hz, 1H), 2.09 (d, J = 12.8 Hz, 2H), 1.31 (s, 3H), 1.24 (s, 3H) ppm.

Table 1 Crystal data and structure refinement summary of **CFA-18**

Empirical formula	$Mn_2Cl_2C_{27}H_{34}N_8O_2$
Formula	$Mn_2Cl_2C_{21}H_{20}N_6(C_3H_7NO)_2$
M_r (g mol^{-1})	683.40
T (K)	100(2)
Wavelength (Å)	0.81040
Crystal system	Trigonal
Space group	$P3_121$ (no. 152)
α (Å)	17.344(3)
γ (Å)	8.807(2)
V (Å^3)	2294.5(9)
Z	3
D_c (g cm^{-3})	1.484
μ (mm^{-1})	1.495
F(000)	1056
Crystal size (mm^3)	0.03 × 0.01 × 0.005
θ range (°)	2.637 to 27.481
Refl. collected	22 416
Refl. unique	2365
Completeness to theta = 27.481° (%)	99.9
Data/restraints/parameters	2365/11/115
R(int)	0.1139
GooF	1.003
Final R indices [$I > 2\sigma(I)$][a]	$R1$ = 0.0999, w$R2$ = 0.2540
R indices (all data)[b]	$R1$ = 0.1607, w$R2$ = 0.3084
Flack parameter	0.04(3)
Largest diff. peak and hole	0.455 and −0.444

[a] $R_1 = \sum||F_o| - |F_c||/\sum|F_o|$. [b] $wR_2 = \sum[w(F_o^2 - F_c^2)2]/\sum[w(F_o^2)2]^{1/2}$.

3,3,3′,3′-Tetramethyl-2,2′,3,3′-tetrahydro-1,1′-spirobi[indene]-6,6′-diyl-bis[(1*R*,2*S*,5*R*)-5-methyl-2-(propan-2-yl)cyclohexyl] biscarbonate (*rac*-2).[47] To a solution of diole *rac*-**1** (17.60 g, 57 mmol), TEA (27.9 mL, 200 mmol) and DMAP (1.22 g, 10 mmol) in dichloromethane (250 mL) along with 25 g (114 mmol) of menthylchloroformate in methylene chloride (10 mL) were added dropwise within 10 min. The mixture was stirred overnight and then washed with HCl, dried with Na_2SO_4, and evaporated to dryness. Yield: 38.3 g (99.6%); M.p.: 130 °C; ^{1}H NMR (400 MHz, $CDCl_3$, 20 °C) δ 7.15 (d, ^3J = 8.3 Hz, 2H), 7.04 (d, ^3J = 8.3 Hz, ^4J = 2.2 Hz, 2H), 6.623 (d, ^4J = 2.0 Hz, 1H), 6.612 (d, ^4J = 2.0 Hz, 1H), 4.61–4.51 (m, 2H$_{menth}$), 2.37 (d, J = 13.2 Hz, 2H), 2.28 (d, J = 13.2 Hz, 1H), 2.26 (d, J = 13.2 Hz, 1H), 2.17–2.10 (m, 2H$_{menth}$), 2.05–1.96 (m, 2H$_{menth}$), 1.72–1.64 (m, 4H$_{menth}$), 1.48–1.44 (m, 4H$_{menth}$), 1.39 (s, 6H), 1.34 (s, 6H), 1.13–1.02 (m, 4H$_{menth}$), 0.92 (d, J = 6.5 Hz, 6H$_{menth}$), 0.91 (d, J = 7.0 Hz, 3H$_{menth}$), 0.90 (d, J = 7.0 Hz, 3H$_{menth}$), 0.89–0.86 (m, 2H$_{menth}$), 0.795 (d, J = 7.0 Hz, 3H$_{menth}$), 0.795 (d, J = 7.0 Hz, 3H$_{menth}$) ppm, specific rotation: −46 ml g^{-1} dm^{-1}.

***aR*-3,3,3′,3′-Tetramethyl-2,2′,3,3′-tetrahydro-1,1′-spirobi[indene]-6,6′-diyl bis[(1*R*,2*S*,5*R*)-5-methyl-2-(propan-2-yl)cyclohexyl] biscarbonate (*aR*-2).**[47] A solution of biscarbonate *rac*-**2** (38.2 g, 56.5 mmol) was stirred in heptane (200 mL) overnight. The precipitate was filtrated, washed two times with cold heptane, and then dried under vacuum. Yield: 13.5 g (96% of theoretical maximum); M.p.: 157 °C; ^{1}H NMR (400 MHz, $CDCl_3$, 20 °C) δ 7.15 (d, ^3J = 8.3 Hz, 1H), 7.04 (dd, ^3J = 8.3 Hz, ^4J = 2.0 Hz, 1H), 6.54 (d, ^4J = 2.0 Hz, 1H), 4.60–4.52 (m, 1H$_{menth}$), 2.37 (d, J = 13.2 Hz, 2H), 2.27 (d, J = 13.2 Hz, 1H), 2.16–2.11 (m, 1H$_{menth}$), 2.04–1.95 (m, 1H$_{menth}$), 1.72–1.64 (m, 2H$_{menth}$), 1.48–1.38 (m, 2H$_{menth}$), 1.39 (s, 3H), 1.34 (s, 3H), 1.13–1.01 (m, 2H$_{menth}$),

0.92 (d, J = 6.5 Hz, $3H_{menth}$), 0.90 (d, J = 7.0 Hz, $3H_{menth}$), 0.89–0.86 (m, $1H_{menth}$), 0.79 (d, J = 7.0 Hz, $3H_{menth}$) ppm; ESI-MS: 1367.90 $[2\ M + Na]^+$, 711.39 $[M + K]^+$, 695.38 $[M + Na]^+$; anal. calcd for $C_{43}H_{60}O_6$: C, 76.75; H, 8.99. Found: C, 62.66; H, 5.00, specific rotation: −2 ml g^{-1} dm^{-1}.

***aR*-3,3,3′,3′-Tetramethyl-5,5′-dinitro-2,2′,3,3′-tetrahydro-1,1′-spirobi[indene]-6,6′-diyl-bis[(1*R*,2*S*,5*R*)-5-methyl-2-(propan-2-yl)cyclohexyl] biscarbonate (*aR*-3).** To a solution of biscarbonate *aR*-**2** (10.56 g, 15.70 mmol) in methylene chloride (320 ml) at 0 °C, nitrating acid [H_2SO_4 (98%)/HNO_3 (65%), 26.0 ml] was added dropwise within 10 min. After stirring for approximately 20 min (TLC). The mixture was quenched with $NaHCO_3$ solution in water to give pure *aR*-**3**. Yield: 11.43 g (96%); M.p.: 159 °C; ^{1}H NMR (400 MHz, $CDCl_3$, 20 °C) δ 7.91 (s, 1H), 6.74 (s, 1H), 4.62–4.56 (m, $1H_{menth}$), 2.47 (d, J = 13.2 Hz, 1H), 2.30 (d, J = 13.2 Hz, 1H), 2.18–2.12 (m, $1H_{menth}$), 2.18–2.04 (m, $1H_{menth}$), 1.73–1.64 (m, $2H_{menth}$), 1.51–1.44 (m, $2H_{menth}$), 1.46 (s, 3H), 1.40 (s, 3H), 1.11–1.01 (m, $2H_{menth}$), 0.92 (d, J = 7.0 Hz, $6H_{menth}$), 0.89–0.86 (m, $1H_{menth}$), 0.81 (d, J = 7.0 Hz, $3H_{menth}$) ppm; ^{13}C (100 MHz, $CDCl_3$, 20 °C) δ 156.0, 152.3, 151.1, 144.4, 141.5, 120.35, 120.29, 120.06, 119.98, 80.82, 80.78, 58.59, 58.51, 58.4, 58.1, 46.9, 44.0, 40.4, 31.4, 31.3, 29.87, 29.82, 25.9, 23.2, 21.9, 20.7, 16.1 ppm; ESI-MS: 1564.02 $[2\ M + K]^+$, 1548.09 $[2\ M + Na]^+$, 801.37 $[M + K]^+$, 785.36 $[M + Na]^+$; anal. calcd for $C_{43}H_{58}N_2O_{10}$: C, 67.69; H, 7.66; N, 3.67. Found: C, 62.66; H, 5.00, specific rotation: *rac*: −14 ml g^{-1} dm^{-1}; *aR*: −10 ml g^{-1} dm^{-1}.

***aR*-3,3,3′,3′-Tetramethyl-5,5′-dinitro-2,2′,3,3′-tetrahydro-1,1′-spirobi[indene]-6,6′-diol (*aR*-4).** A suspension of dinitro-biscarbonate *aR*-**3** (11.18 g, 14.65 mmol) and hydrazine hydrate (5.13 ml, 5.23 g, 163 mmol) in THF (150 ml) was heated under reflux for 4 h. After cooling to 20 °C, the pure product precipitated as an orange solid, which was collected by filtration, washed with cold THF, and dried for 15 h in an oven at 65 °C to obtain the product as a yellow solid. Yield: 5.68 g (97%); M.p.: 213 °C; ^{1}H NMR (400 MHz, $CDCl_3$, 20 °C): δ 10.60 (s, 2H), 7.91 (s, 2H), 6.54 (s, 2H), 2.43 (d, J = 13.2 Hz, 2H), 2.28 (d, J = 13.2 Hz, 2H), 1.44 (s, 6H), 1.37 (s, 6H) ppm; ^{13}C (100 MHz, $CDCl_3$, 20 °C, BB515_C): δ 160.5, 155.3, 145.1, 133.5, 118.7, 118.6, 114.9, 114.8, 58.8, 58.7, 58.6, 58.2, 43.4, 31.7, 31.6, 30.1, 30.0 ppm; ESI-MS: 421.15 $[M + Na]^+$, 819.26 $[2M + Na]^+$; anal. calcd for $C_{21}H_{22}N_2O_6$: C, 62.66; H, 5.00; N, 7.31. Found: C, 62.66; H, 5.00; N, 7.31, specific rotation: −7 ml g^{-1} dm^{-1}.

***aR*-3,3,3′,3′-Tetramethyl-5,5′-dinitro-2,2′,3,3′-tetrahydro-1,1′-spirobi[indene]-6,6′-diamine (*aR*-5).** A mixture of nitrophenol *aR*-**4** (2.87 g, 7.21 mmol), potassium carbonate (5.07 g, 36.05 mmol), 2-chloroacetamide (1.62 g, 17.33 mmol), potassium iodide (478 mg, 2.88 mmol), and DMF (100 ml) was heated at 90 °C for 2 h and then at 150 °C for 4 h. Subsequently, the DMF was removed by distillation at 10 mbar. Pure product (1.89 g, 4.77 mmol, 66%) in the form of an orange solid was obtained by subjecting the residue to column chromatography (cyclohexane/EtOAc, 4 : 1). Yield: 1.87 g (65%) M.p.: 330 °C; ^{1}H NMR (400 MHz, $CDCl_3$, 20 °C) δ 7.92 (s, 1H), 6.23 (s, 1H), 2.37 (d, J = 13.2 Hz, 1H), 2.21 (d, J = 13.2 Hz, 1H), 1.40 (s, 3H), 1.34 (s, 3H) ppm; ^{13}C (100 MHz, $CDCl_3$, 20 °C, LK_10_1-C) δ 159.4, 144.8, 142.5, 132.4, 119.57, 119.48, 113.49, 113.34, 59.0, 57.7, 43.1, 31.64, 31.58, 30.22, 30.16 ppm; ^{13}C NMR (100 MHz, $CDCl_3$, d_4-methanol 9 : 1, 20 °C, BB497_C) δ 159.6, 145.5, 142.1, 131.8, 119.13, 119.11, 113.48, 113.44, 58.9, 57.6, 42.9, 31.4, 30.0 ppm; ESI-MS: 419.18 $[M + Na]^+$; anal. calcd for $C_{21}H_{24}N_4O_4$: C, 63.62; H, 6.10; N, 14.13. Found: C, 62.66; H, 5.00; N, 7.31, specific rotation: 138 ml g^{-1} dm^{-1}.

***aR*-3,3,3′,3′-Tetramethyl-2,2′,3,3′-tetrahydro-1,1′-spirobi[indene]-5,5′,6,6′-tetraamine (*aR*-6).** Nitroaniline *aR*-**5** (1.87 g, 4.72 mmol) was hydrogenated at room temperature in ethanol (150 ml) with 5% palladium on charcoal and hydrogen (5 bar) for 48 h. The catalyst was removed by filtration under nitrogen atmosphere, and the solvent was evaporated under vacuum to obtain air-sensitive tetraamine as a colorless solid, which was directly used in the next reaction step. ^{1}H NMR (400 MHz, d_4-methanol, 20 °C) δ 6.53 (s, 1H), 6.15 (s, 1H), 2.20 (d, J = 13.2 Hz, 1H), 2.08 (d, J = 13.2 Hz, 1H), 1.30 (s, 3H), 1.24 (s, 3H) ppm. ^{13}C NMR (100 MHz, d_4-methanol, 20 °C) δ 143.7, 145.5, 133.8, 112.1, 112.0, 109.5, 109.40, 59.9, 56.7, 42.4, 30.89, 30.84, 29.58, 29.52 ppm; ESI-MS: 711.43 $[2\ M + K]^+$, 695.46 $[2\ M + Na]^+$, 375.23 $[M + K]^+$, 359.25 $[M + Na]^+$, 337.27 $[M + H]^+$.

***aR*-7,7,7′,7′-Tetramethyl-6,6′,7,7′-tetrahydro-1*H*,3′*H*-5,5′-spirobi[indeno[5,6-*d*][1,2,3]triazole] (*aR*-7).** Under nitrogen atmosphere, the crude tetraamine *aR*-**6** was dissolved in acetic acid (80 ml) and water (20 ml) and cooled to 0 °C. A solution of sodium nitrite (1.13 g, 16.38 mmol) in water (5 mL) was then added dropwise while keeping the temperature of the mixture below 5 °C. The resulting solution was stirred at 0 °C for additional 30 min followed by the addition of water (400 mL). The precipitate was isolated by filtration, washed with water, and dried. The crude product was purified by column chromatography ($CHCl_3$/MeOH 9 : 1) to give pure bistriazole 7 as a colorless solid. Yield: 1.38 g (82%, two steps from *aR*-**5**) M.p.: 322 °C; ^{1}H NMR (400 MHz, d_6-DMSO, 20 °C, 517_S_H_RT) δ 15.55 (s, 1H), 15.33 (s, 1H), 7.87 (s, 1H), 7.56 (s, 1H), 7.26 (s, 1H), 6.96 (s, 1H), 2.50 (d, J = 12.5 Hz, 2H), 2.46 (d, J = 12.5 Hz, 2H), 1.48 (s, 6H), 1.39 (s, 6H) ppm; ^{1}H NMR (100 MHz, d_6-DMSO, 80 °C, 517_S_H_80 °C) δ 15.19 (s, 2H), 7.69 (s, 2H), 7.11 (s, 2H), 2.53 (d, J = 13.1 Hz, 2H), 2.42 (d, J = 13.1 Hz, 2H), 1.51 (s, 6H), 1.43 (s, 6H) ppm; ^{1}H NMR (400 MHz, $CDCl_3$, d_4-methanol 9 : 1, 20 °C, LK_12a) δ 7.59 (s, 2H), 7.15 (s, 2H), 2.58 (d, J = 13.1 Hz, 2H), 2.42 (d, J = 13.1 Hz, 2H), 1.51 (s, 6H), 1.44 (s, 6H) ppm. ^{13}C NMR (100 MHz, $CDCl_3$, d_4-methanol 9 : 1, 20 °C, LK-12_1R_ca) δ 152.4, 151.9, 139.6, 138.9, 109.51, 109.46, 107.36, 107.24, 60.3, 56.6, 43.0, 32.12, 32.08, 30.46, 30.37 ppm; IR (cm^{-1}): 2951 (m), 2924 (m), 2856 (m), 1726 (b), 1628 (m), 1584 (m), 1500 (w), 1463 (m), 1365 (m), 1316 (w), 1295 (w), 1257 (m), 1190 (st), 1071 (m), 993 (m), 850 (st), 803 (st), 750 (st), 634 (b), 592 (w), 562 (w), 540 (st), 475 (st), 410 (st); ESI-MS: 739.33 $[2\ M + Na]^+$, 381.17 $[M + Na]^+$; anal. calcd for $C_{21}H_{22}N_6$: C, 70.37; H, 6.19; N, 23.45. Found: C, 62.66; H, 5.00; N, 7.31, specific rotation: 167 ml g^{-1} dm^{-1}.

MOF synthesis

Synthesis of [Mn_2Cl_2(*spirta*)(DMF)2] (8). In a glass tube (10 mL) the solution of *H_2-spirta* (10 mg, 0.028 mmol) in DMF (1 mL) was added to a solution of manganese(II) chloride dihy-

drate (18 mg, 0.117 mmol) in DMF (1 mL) and mixed thoroughly. This Tube was closed with a plastic cap and the mixture was heated to 140 °C for three days and subsequently filtrated. The colorless crystals were washed with ethanol three times. After vacuum drying at 100 °C, a white powder results. Yield: 6 mg (57%); IR (cm^{-1}): 2953 (w), 2931 (w), 2860 (w), 1658 (vst), 1563 (w), 1458 (m), 1381 (m), 1363 (w), 1316 (w), 1251 (w), 1177 (st), 1111 (m), 1059 (w), 862 (st), 808 (st), 733 (m), 678 (st), 564 (w), 547 (w), 490 (w). Anal. calcd for $[Mn_2Cl_2(C_{21}H_{22}N_6)(C_3H_7NO)_2]$: C, 47.45; H, 4.97; N, 16.40. Found: C, 45.18; H, 4.48; N, 15.05.

Conflicts of interest

There are no conflicts to declare.

Notes and references

1 A. J. Rieth, Y. Tulchinsky and M. Dincă, *J. Am. Chem. Soc.*, 2016, **138**, 9401–9404.

2 (*a*) P.-Q. Liao, H. Chen, D.-D. Zhou, S.-Y. Liu, C.-T. He, Z. Rui, H. Ji, J.-P. Zhang and X.-M. Chen, *Energy Environ. Sci.*, 2015, **8**, 1011–1016; (*b*) M. Dinca, A. F. Yu and J. R. Long, *J. Am. Chem. Soc.*, 2006, **128**, 8904–8913.

3 S. Biswas, M. Grzywa, H. P. Nayek, S. Dehnen, I. Senkovska, S. Kaskel and D. Volkmer, *Dalton Trans.*, 2009, 6487–6495.

4 J. Teufel, H. Oh, M. Hirscher, M. Wahiduzzaman, L. Zhechkov, A. Kuc, T. Heine, D. Denysenko and D. Volkmer, *Adv. Mater.*, 2013, **25**, 635–639.

5 G. Sastre, J. van den Bergh, F. Kapteijn, D. Denysenko and D. Volkmer, *Dalton Trans.*, 2014, **43**, 9612–9619.

6 B. Paschke, D. Denysenko, B. Bredenkötter, G. Sastre, A. Wixforth and D. Volkmer, *Chem. – Eur. J.*, 2019, **25**, 10803–10807.

7 B. Paschke, A. Wixforth, D. Denysenko and D. Volkmer, *ACS Sens.*, 2017, **2**, 740–747.

8 (*a*) D. Denysenko, M. Grzywa, J. Jelic, K. Reuter and D. Volkmer, *Angew. Chem.*, 2014, **126**, 5942–5946; (*b*) R. Röß-Ohlenroth, B. Bredenkötter and D. Volkmer, *Organometallics*, 2019, **38**, 3444–3452.

9 D. Denysenko and D. Volkmer, *Faraday Discuss.*, 2017, **201**, 101–112.

10 C. Wang, T. Zhang and W. Lin, *Chem. Rev.*, 2012, **112**, 1084–1104.

11 X.-L. Yang and C.-D. Wu, *CrystEngComm*, 2014, **16**, 4907–4918.

12 (*a*) J. S. Seo, D. Wang, H. Lee, S. I. Jun, J. Oh, Y. J. Yeon and K. Kim, *Nature*, 2000, **404**, 982–986; (*b*) A. P. Katsoulidis, D. Antypov, G. F. S. Whitehead, E. J. Carrington, D. J. Adams, N. G. Berry, G. R. Darling, M. S. Dyer and M. J. Rosseinsky, *Nature*, 2019, **565**, 213–217; (*c*) J. Navarro-Sánchez, A. I. Argente-García, Y. Moliner-Martínez, D. Roca-Sanjuán, D. Antypov, P. Campíns-Falcó, M. J. Rosseinsky and C. Martí-Gastaldo, *J. Am. Chem. Soc.*, 2017, **139**, 4294–4297; (*d*) S.-Y. Zhang, C.-X. Yang, W. Shi, X.-P. Yan, P. Cheng, L. Wojtas and M. J. Zaworotko, *Chem*, 2017, **3**, 281–289; (*e*) M. N. Corella-Ochoa, J. B. Tapia, H. N. Rubin, V. Lillo, J. González-Cobos, J. L. Núñez-Rico, S. R. G. Balestra, N. Almora-Barrios, M. Lledós, A. Güell-Bara, J. Cabezas-Giménez, E. C. Escudero-Adán, A. Vidal-Ferran, S. Calero, M. Reynolds, C. Martí-Gastaldo and J. R. Galán-Mascarós, *J. Am. Chem. Soc.*, 2019, **141**, 14306–14316.

13 C. Zhuo, Y. Wen and X. Wu, *CrystEngComm*, 2016, **18**, 2792–2802.

14 J. Zhang, J. Jin, R. Cooney, Q. Fu, G. G. Qiao, S. Thomas and T. C. Merkel, *Polym. Chem.*, 2015, **6**, 5003–5008.

15 J. D. Evans, B. Garai, H. Reinsch, W. Li, S. Dissegna, V. Bon, I. Senkovska, R. A. Fischer, S. Kaskel, C. Janiak, N. Stock and D. Volkmer, *Coord. Chem. Rev.*, 2019, **380**, 378–418.

16 M. Yoon, R. Srirambalaji and K. Kim, *Chem. Rev.*, 2012, **112**, 1196–1231.

17 Y. Liu, W. Xuan and Y. Cui, *Adv. Mater.*, 2010, **22**, 4112–4135.

18 P. Schmieder, D. Denysenko, M. Grzywa, B. Baumgärtner, I. Senkovska, S. Kaskel, G. Sastre, L. van Wüllen and D. Volkmer, *Dalton Trans.*, 2013, **42**, 10786–10797.

19 R. E. Morris and X. Bu, *Nat. Chem.*, 2010, **2**, 353–361.

20 S.-Y. Zhang, D. Li, D. Guo, H. Zhang, W. Shi, P. Cheng, L. Wojtas and M. J. Zaworotko, *J. Am. Chem. Soc.*, 2015, **137**, 15406–15409.

21 Q. Zhu, T. Sheng, R. Fu, C. Tan, S. Hu and X. Wu, *Chem. Commun.*, 2010, **46**, 9001–9003.

22 (*a*) X. Zhao, E. T. Nguyen, A. N. Hong, P. Feng and X. Bu, *Angew. Chem.*, 2018, **130**, 7219–7223; (*b*) Z.-G. Gu, C. Zhan, J. Zhang and X. Bu, *Chem. Soc. Rev.*, 2016, **45**, 3122–3144.

23 Z.-X. Xu, Y.-X. Tan, H.-R. Fu, Y. Kang and J. Zhang, *Chem. Commun.*, 2015, **51**, 2565–2568.

24 (*a*) C. Martí-Gastaldo, J. E. Warren, K. C. Stylianou, N. L. O. Flack and M. J. Rosseinsky, *Angew. Chem., Int. Ed.*, 2012, **51**, 11044–11048; (*b*) A. P. Katsoulidis, K. S. Park, D. Antypov, C. Martí-Gastaldo, G. J. Miller, J. E. Warren, C. M. Robertson, F. Blanc, G. R. Darling, N. G. Berry, J. A. Purton, D. J. Adams and M. J. Rosseinsky, *Angew. Chem., Int. Ed.*, 2014, **53**, 193–198.

25 C. Martí-Gastaldo, D. Antypov, J. E. Warren, M. E. Briggs, P. A. Chater, P. V. Wiper, G. J. Miller, Y. Z. Khimyak, G. R. Darling, N. G. Berry and M. J. Rosseinsky, *Nat. Chem.*, 2014, **6**, 343–351.

26 C. Martí-Gastaldo, J. E. Warren, M. E. Briggs, J. A. Armstrong, K. M. Thomas and M. J. Rosseinsky, *Chem. – Eur. J.*, 2015, **21**, 16027–16034.

27 F. Xia, M. Pan, S. Mu, R. Malpass-Evans, M. Carta, N. B. McKeown, G. A. Attard, A. Brew, D. J. Morgan and F. Marken, *Electrochim. Acta*, 2014, **128**, 3–9.

28 M.-J. Lin, A. Jouaiti, N. Kyritsakas and M. W. Hosseini, *Chem. Commun.*, 2010, **46**, 115–117.

29 S. Biswas, M. Tonigold, M. Speldrich, P. Kögerler, M. Weil and D. Volkmer, *Inorg. Chem.*, 2010, **49**, 7424–7434.

30 D. Denysenko, M. Grzywa, M. Tonigold, B. Streppel, I. Krkljus, M. Hirscher, E. Mugnaioli, U. Kolb, J. Hanss and D. Volkmer, *Chem. – Eur. J.*, 2011, **17**, 1837–1848.

31 P.-Q. Liao, X.-Y. Li, J. Bai, C.-T. He, D.-D. Zhou, W.-X. Zhang, J.-P. Zhang and X.-M. Chen, *Chem. – Eur. J.*, 2014, **20**, 11303–11307.

32 N. L. Rosi, J. Kim, M. Eddaoudi, B. Chen, M. O'Keeffe and O. M. Yaghi, *J. Am. Chem. Soc.*, 2005, **127**, 1504–1518.

33 P. D. C. Dietzel, Y. Morita, R. Blom and H. Fjellvåg, *Angew. Chem., Int. Ed.*, 2005, **44**, 6354–6358.

34 V. Kumar, S. Chatterjee, P. Sharma, S. Chakrabarty, C. V. Avadhani and S. Sivaram, *J. Polym. Sci., Part A: Polym. Chem.*, 2018, **56**, 1046–1057.

35 L. A. Nafie, *Vibrational optical activity. Principles and applications*, Wiley, Chichester England, Syracuse, N.Y, 2011.

36 P. J. Stephens, F. J. Devlin and J. R. Cheeseman, *VCD spectroscopy for organic chemists*, CRC Press, Boca Raton, 2012.

37 (*a*) H. D. Flack and G. Bernardinelli, *Acta Crystallogr., Sect. A: Found. Crystallogr.*, 1999, **55**, 908–915; (*b*) H. D. Flack and G. Bernardinelli, *Chirality*, 2008, **20**, 681–690.

38 *Spartan*, Wavefunction Inc., 18401 Von Karman Avenue, Suite 370, Irvine, CA 92612, USA.

39 M. J. Frisch, G. W. Trucks, H. B. Schlegel, G. E. Scuseria, M. A. Robb, J. R. Cheeseman, G. Scalmani, V. Barone, G. A. Petersson, H. Nakatsuji, X. Li, M. Caricato, A. V. Marenich, J. Bloino, B. G. Janesko, R. Gomperts, B. Mennucci, H. P. Hratchian, J. V. Ortiz, A. F. Izmaylov, J. L. Sonnenberg and D. Williams-Young, *Gaussian 16*, Gaussian Inc., Wallingford CT, 2016.

40 J. Tomasi, B. Mennucci and R. Cammi, *Chem. Rev.*, 2005, **105**, 2999–3093.

41 (*a*) J. M. Batista, E. W. Blanch and V. D. S. Bolzani, *Nat. Prod. Rep.*, 2015, **32**, 1280–1302; (*b*) T. B. Freedman, X. Cao, R. K. Dukor and L. A. Nafie, *Chirality*, 2003, **15**, 743–758; (*c*) P. L. Polavarapu and C. L. Covington, *Chirality*, 2014, **26**, 539–552; (*d*) J. Bogaerts, F. Desmet, R. Aerts, P. Bultinck, W. Herrebout and C. Johannessen, *Phys. Chem. Chem. Phys.*, 2020, **22**, 18014–18024; (*e*) C. Merten, T. P. Golub and N. M. Kreienborg, *J. Org. Chem.*, 2019, **84**, 8797–8814.

42 P.-E. Werner, L. Eriksson and M. Westdahl, *J. Appl. Crystallogr.*, 1985, 367–370.

43 L. Sarkisov and A. Harrison, *Mol. Simul.*, 2011, **37**, 1248–1257.

44 D. Dubbeldam, S. Calero and T. J. H. Vlugt, iRASPA: GPU-accelerated visualization software for materials scientists, *Mol. Simul.*, 2018, **44**, 653–676.

45 A. J. Howarth, A. W. Peters, N. A. Vermeulen, T. C. Wang, J. T. Hupp and O. K. Farha, *Chem. Mater.*, 2016, **29**, 26–39.

46 S. Sasaki, K. Fujino and Y. Takéuchi, *Proc. Jpn. Acad., Ser. B*, 1979, **55**, 43–48.

47 T. R. Welter, *WO* 2006/019663, 2005.

48 X. Ma, R. Swaidan, Y. Belmabkhout, Y. Zhu, E. Litwiller, M. Jouiad, I. Pinnau and Y. Han, *Macromolecules*, 2012, **45**, 3841–3849.

49 G. M. Sheldrick, *Acta Crystallogr., Sect. C: Struct. Chem.*, 2015, **71**, 3–8.